# Influence of precursor concentration and deposition temperature on the photoactivity of hematite electrodes for water splitting

Justine Sageka Nyarige, Tjaart P.J. Krüger and Mmantsae Diale

Department of Physics, University of Pretoria, Private Bag X20, Hatfield 0028, South Africa

* Corresponding author. mmantsae.diale@up.ac.za

## Abstract

Hematite nanoparticles were synthesized using chemical spray pyrolysis. Precursor concentrations of 30, 40, and 50 mM, deposition temperatures of 250, 340, and 400 °C were used. X-ray diffraction measurements confirmed the purity of hematite with no other phases of iron oxide. The (104) and (110) diffraction peaks associated with corundum structure of hematite were revealed in all the prepared thin films. The rhombohedral unit cell with space group $R\bar{3}C$ and average lattice constants, $a = 5.042$ Å and $c = 13.673$ Å were achieved. Scanning electron microscopy measurements obtained surface morphology of different grain sizes that ranged from 7 to 33 nm. From the UV–vis measurements, bandgaps that ranged from 2.10 to 1.92 eV for all films prepared at different precursor concentrations and temperatures were obtained. Photocurrent densities that ranged from 0.78 to 89 μA $cm^{-2}$ were obtained for different precursor concentrations and deposition temperatures thin films. Further, all the samples had a donor density of $10^{18}$ $cm^{-3}$ with a positive flat band potential in the range of 0.045 and 0.213 V.

## Graphical abstract

Materials Energy Today manuscript images (J.S.N).

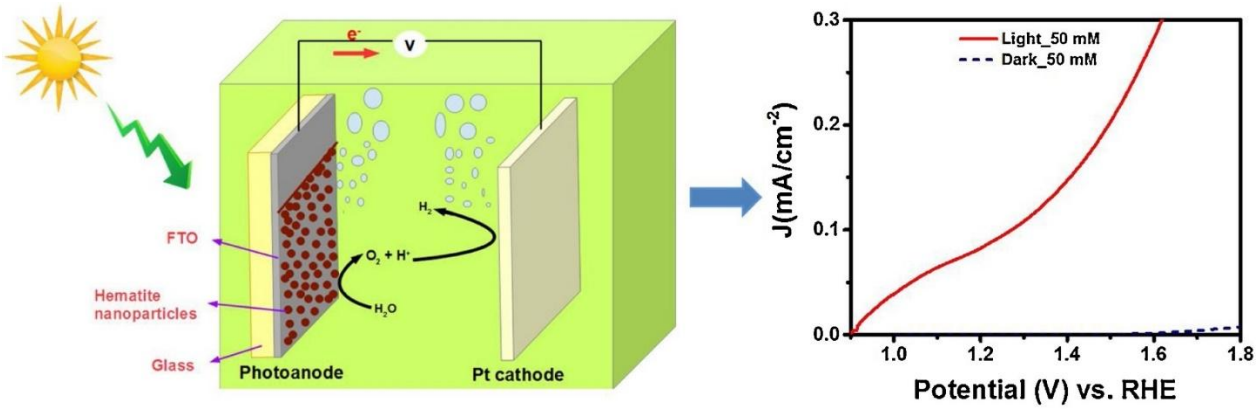


**Keywords**

Hematite nanoparticles
Chemical spray pyrolysis
Photocurrent
Water splitting

## 1. Introduction

The global energy demand has been on the rise due to the increase in world population. The annual energy consumption is estimated at 17.7 TW, with fossil fuels being the main source accounting for 87% of the total energy produced [1], [2]. Solar energy that irradiates the earth at any given moment is approximately $1.4 \times 10^5$ TW which is higher by four orders of magnitude of the global energy consumption. Of this energy received from the sun, about $3.6 \times 10^4$ TW is usable [3]. Efficient utilization of solar energy, therefore, will help reduce the excess $CO_2$ emission and hence saving our environment. However, sunlight is intermittent and varies irregularly over the day, year, and place on earth. This, therefore, implies that better storage of harvested energy is of utmost importance [4]. The hydrogen economy has recently been under study as one of the solutions for the post-carbon future as solar energy storage. For this vision to be realized, efficient and inexpensive ways of hydrogen production have to be developed [5]. Hydrogen fuel, just like fossil fuels, can also be used in homes, industry, and transport [5]. The advantage of hydrogen as compared to other fossil fuels is that the only by-product produced is water.

One of the approaches that have been used in the production of hydrogen is photoelectrochemical (PEC) water splitting [6]. The PEC cell uses semiconductors as photoanodes and platinum as a counter electrode in splitting water, producing hydrogen and oxygen [7]. Fujishima and Honda were the first researchers to the PEC water splitting using crystalline $TiO_2$ (rutile) anode and platinum cathode under UV irradiation [8]. However, the efficiency of hydrogen production was low because of the large band gap of titanium dioxide ($TiO_2$) of 3.2 eV which is in the UV region [9]. Since then, $WO_3$, $BiVO_4$, $Cu_2O$, CuO, ZnO, CdS, $MoS_2$ and $Fe_2O_3$ materials have been explored for suitability in PEC water splitting [10], [11], [12], [13], [14], [15], [16], [17], [18]. Of these semiconductors, hematite has attracted much attention as a promising candidate for PEC applications, due to good absorption in the visible region resulting from a low indirect bandgap in the range of 1.90–2.20 eV. This bandgap corresponds to wavelengths between 650 nm and 560 nm respectively [19], which can achieve a theoretical solar-to-hydrogen (STH) efficiency of 15% [20]. In addition, hematite is chemically stable under aqueous environment, relatively abundant, non-toxic, and can be prepared from inexpensive reagents using simple deposition techniques [21]. Bard and Hartee were the first researchers to report on hematite using chemical vapor deposition [22]. For efficient water splitting, electrons move to the photoanode (hematite) where oxidation of water into oxygen gas takes place while the holes move to the counter electrode (platinum) where reduction of water to hydrogen occurs. Conversely, an external bias is needed for hydrogen generation to start taking place. This is due to conduction band which is more positive (0.4 V *vs*. RHE) relative to the hydrogen evolution reaction (HER) [23], [24]. Other drawbacks of hematite as a photoanode include poor electronic properties such as low hole mobility, poor conductivity and short electron–hole (e–h) diffusion length [25], [26] leading to high e-h recombination, generated according to the equation, $Fe_2O_3 + h\nu \longrightarrow 2(Fe_2O_3)e^- + 2(Fe_2O_3)h^+$ and hence limiting water splitting process [27].

Nanostructured hematite such as nanowires [28], nanotubes [29] and dendrites [30] have been reported to improve the photocurrent production. The reduction of the grain sizes of the nanostructures improves the carrier collection [31]. This enhances the interfacial reaction area in which the minority carriers travel, thereby avoiding the e–h recombination that results from the short diffusion path of the holes to the nanostructured material surface. For this to effectively happen, the grain sizes of the nanostructures should be comparable to the

diffusion length of the holes (2–4 nm)[32]. However, the influence of the thickness of nanostructures on optical absorption is not well known.

Different methods have been used to synthesize hematite nanostructures, which influence the structural, morphological, optical, and electrical properties of the produced films. Some of the reported methods include chemical bath deposition [33], spin coating [34], dip coating [35], hydrothermal [36] and spray pyrolysis [37]. Among these, chemical spray pyrolysis (CSP) has been revealed to produce desirable films for charge transport [38]. Moreover, CSP is a simple and cheap process to produce large-area thin films without wasting the material. In addition, various parameters like temperature, concentration, and deposition time can be optimized, producing different stoichiometric films for different applications [39].

In this study, hematite nanoparticles were synthesized using CSP. Different precursor concentrations ranging from 30 to 50 mM, and substrate temperatures of 250 °C, 340 °C and 400 °C were used. The effect of precursor concentration and temperature on structural, morphological, optical, and electrical properties is reported. This study aims at investigating the effect of precursor concentrations and deposition temperatures in preparation of hematite thin films using spray pyrolysis for PEC water splitting.

## 2. Experimental details

Fig. 1 presents the CSP setup. Iron nitrate nonahydrate, $Fe(NO_3).9H_2O$ (Sigma Aldrich) was used as the precursor and fluorine-doped tin oxide ($SnO_2$:F) on glass as the substrate. Precursor concentrations of 30, 40, and 50 mM were dissolved in deionized water to form a homogeneous solution. 5 ml of ethanol was then added to the solution to increase the evaporation rate during CSP deposition at a constant temperature of 280 °C. The nozzle to substrate distance was 22 cm, spray pressure of $2.2 \times 10^5$ Pa, and, nozzle diameter of 0.3 mm were all kept constant during deposition. The 50 mM precursor was used to prepare NPs at temperatures of 250, 340, and 400 °C. All the samples were annealed at 450 °C for 1 h and allowed to cool for 10 h to room temperature.

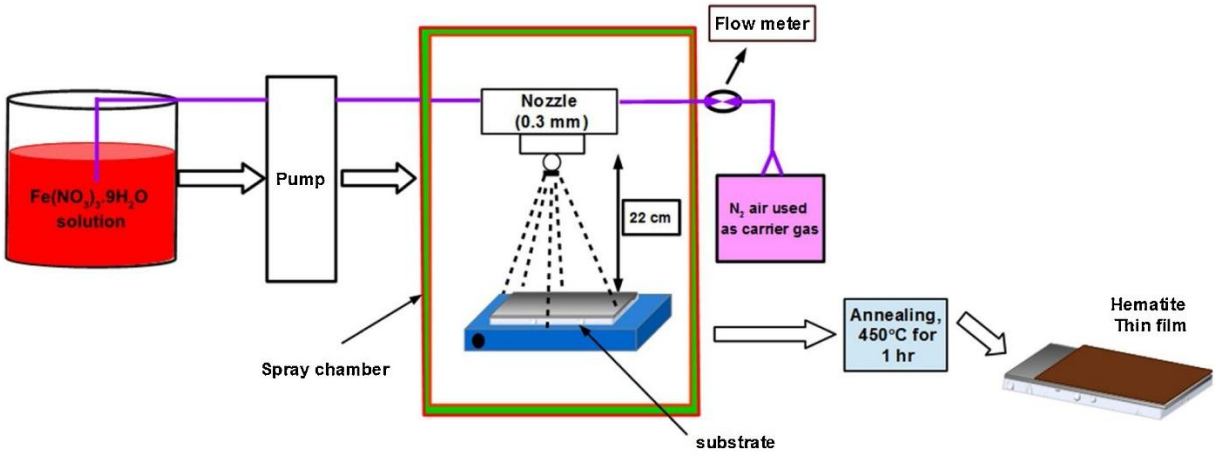


**Fig. 1.** Schematic diagram of spray pyrolysis used for synthesis of hematite nanostructures at different precursor concentrations and deposition temperatures.

A field emission scanning electron microscope (Zeiss Crossbeam 540 FESEM-Microscopes) operating at 2 kV was used to determine the surface morphology of hematite NPs. The grain sizes of the synthesized NPs were estimated using ImageJ. Additionally, Gaussian fitting and

histogram were used to obtain the frequency of the nanoparticle size distribution. The crystal structure of all the samples was confirmed using Bruker D2 Phaser X-ray diffractometer (XRD), with a 0.15418 nm source, and $CuK_{\alpha}$ radiation, for $2\theta$ range of 20°–70° [40]. Cary 100 Bio UV–vis spectrophotometer was used to measure the absorbance.

Photocurrent density measurements were carried out in a 'Cappucino cell' using the potentiostat (VersaSTAT 3F, U.S.A). Hematite was used as a working electrode, platinum mesh as a counter electrode and 3.0 M KCl saturated Ag/AgCl as a reference electrode. Photocurrent readings as a function of applied voltage using 1.0 M NaOH, pH 13.8 as the electrolyte, with a scan rate of 50 mV $s^{-1}$ were recorded. For light measurements, the simulated sun was irradiated to a 0.49 $cm^2$ area of hematite photoanode using solar simulator (Newport LSC 100 W Xenon lamp), with AM 1.5 G filter adjusting the power of the lamp [40]. The light intensity of photoanodes (hematite) location in the photoelectrochemical cell was measured by the detector (Newport) was 100 $Wcm^{-2}$. The Nernst equation was used to convert all the potentials obtained to a reversible hydrogen electrode (RHE),

$$E_{\mathrm{RHE}} = E_{(\mathrm{Ag\,/\,AgCl})} + 0.059\mathrm{PH} + E^{\circ}{}_{(\mathrm{Ag\,/\,AgCl})} \quad (1)$$

where $E°_{(Ag/AgCl)}$ is 0.205 V at 25°, and $E_{(Ag/AgCl)}$ is the potential against reference electrode (Ag/AgCl) measured experimentally [41], [42].

## 3. Results and discussion

### 3.1. X-ray diffraction

Fig. 2 represents well-defined diffraction XRD patterns of hematite that were indexed at their right $2\theta$ positions (JCPDS. No 33-0664). The peak intensities were observed to increase slightly as the precursor concentrations and temperatures were varied from 30 to 50 mM and 250 to 400 °C respectively. This could be due to the change in phase from amorphous to polycrystalline. The Miller indices of (012), (104), (110), (113), (024), (116), (214) were indexed at 24.3°, 33.3°, 35.8°,41.0°, 49.6°, 54.2°, and 64.1° respectively. The peaks obtained corresponded to the standard hematite pattern. The (012), (104), and (110) were further the dominant peaks in all samples. These peaks are characteristic of the rhombohedral hematite structure with space group $R\bar{3}C$[43], [44]. Crystallite size of hematite thin film was obtained using the Debye-Scherrer's equation,

$$D = \frac{0.9\lambda}{\beta \cos\theta}, \quad (2)$$

where $\lambda$ is the wavelength of X-ray source and $\beta$ the full width at half maximum [45].

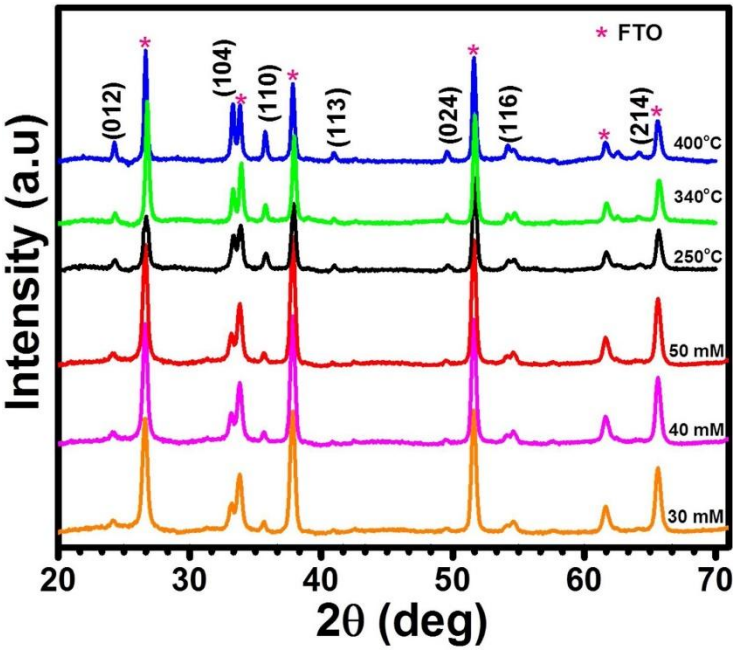


**Fig. 2**. XRD of hematite samples prepared by spray pyrolysis at different precursor concentrations and deposition temperatures.

The crystal size of hematite thin films at different concentrations increased from 23.05 to 29.92 nm, while for different temperatures, there was a reduction in the crystal size from 38.11 to 23.97 nm. This change is attributed to crystallinity for different temperatures and precursor concentrations. The three dominant peaks; (012), (104), (110) were used to calculate the lattice constants. The lattice constants, *a*, *b* and *c*, were determined by the following relations,

$$2d_{\mathrm{hkl}} \sin\theta = n\lambda, \quad (3)$$

And

$$\frac{1}{d_{\mathrm{hkl}}^2} = \frac{4}{3a^2}\left(h^2 + k^2 + \mathrm{hk}\right) + \frac{l^2}{c^2}, \quad (4)$$

where $d_{hkl}$ and (*hkl*) are the inter-planar spacing between crystal planes and Miller indices respectively [46]. The average *a* and *c* obtained for different molar concentrations were 5.0681 Å and 13.6934 Å while 5.0172 Å and 13.6527 Å were obtained for samples deposited at different temperatures, shown in Fig. 3. These results agree with the standard lattice parameters (5.0346 Å and 13.752 Å from JCPDS card no 33-0664 for hematite. The small variation could be due to the substrate influence on the growth of thin films. A similar trend has been reported by Sharma et al. on the reversal in the lattice parameters of hematite thin films [47].

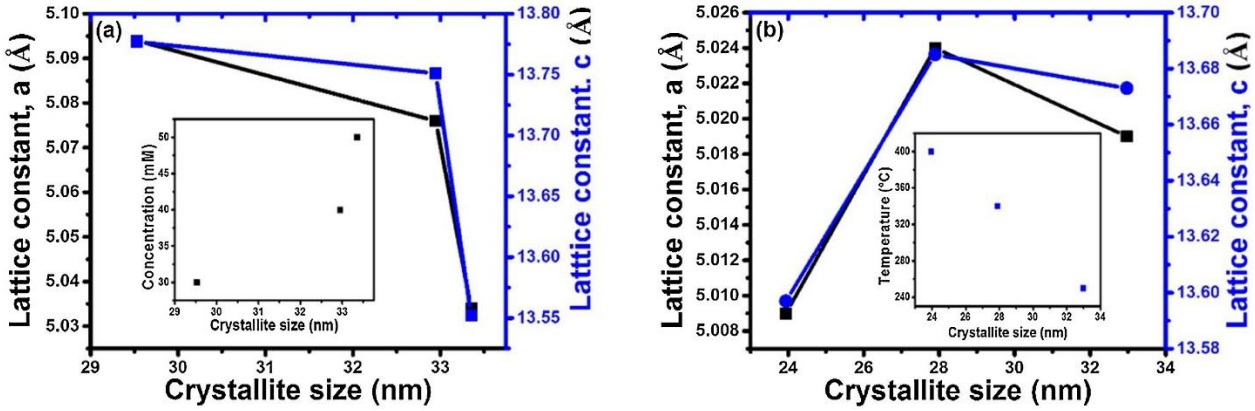


**Fig. 3**. Lattice constants (a, c) and crystallite sizes for hematite samples prepared samples prepared by spray pyrolysis at different precursor concentration and deposition temperatures. The inset in (a) and (b) shows the variation of temperature and concentration with crystallite sizes respectively.

### 3.2. Morphology of hematite nanoparticles

Fig. 4 represents the surface morphology of hematite thin films. Samples prepared at different precursor concentrations showed an increase in grain size as the concentration was varied from 30 to 50 mM, attributed to the aggregation of the precursor (iron nitrate nonahydrate) during synthesis. We believe that this aggregation further led to the agglomeration hence increasing the grain size at higher precursor concentrations.

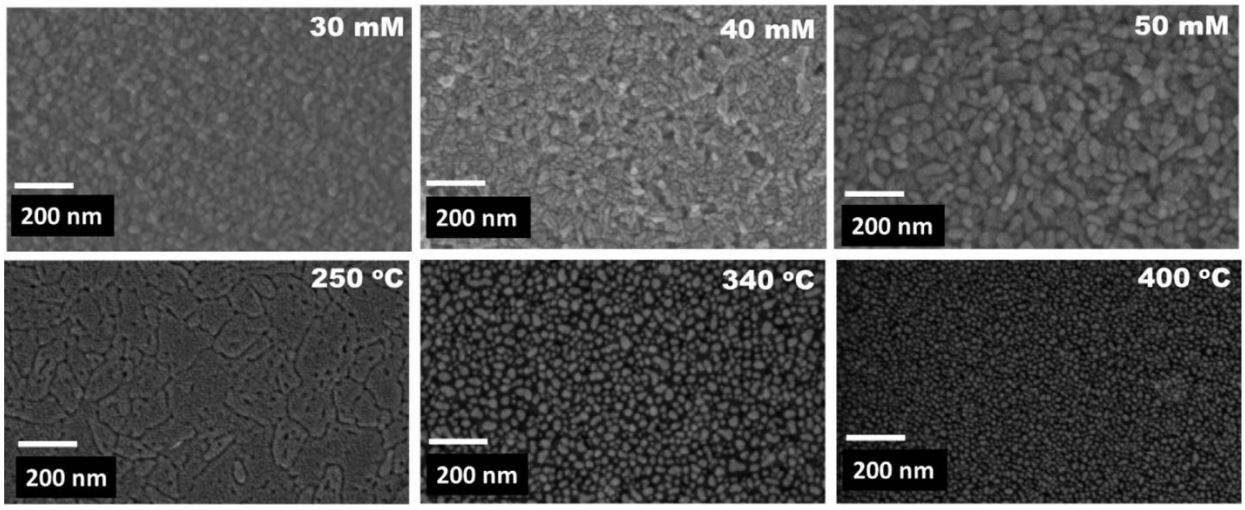


**Fig. 4**. Scanning electron microscopy micrographs of nanostructured hematite thin films prepared by spray pyrolysis at different deposition temperatures and molar concentrations.

Iron nuclei content was created during aggregation, hence limiting the grain sizes. Fouad et al. reported similar results on hematite using precipitation, with a variation of the precursor concentrations and its effect on the grain size, morphology, lumps formation, and crystallinity [48]. From their findings, they observed a lot of agglomerations and lumps of the grain size with an increase in precursor concentration. Additionally, grain sizes calculated using ImageJ were observed to decrease from 33 to 14 nm as the deposition temperature increased from 250 to 400 °C, attributed to high evaporation rate at higher temperatures, resulting in the deposition in a vapor form while at lower temperatures (250 °C), the deposition only took place in liquid form. A similar study was reported by us on the structural and optical

properties of L-arginine/hematite nanostructures prepared by both spray pyrolysis and chemical bath deposition [41]. The average grain size of hematite thin films at different concentrations increased from 7 to 19 nm as shown in Figs. 5 and 6 .

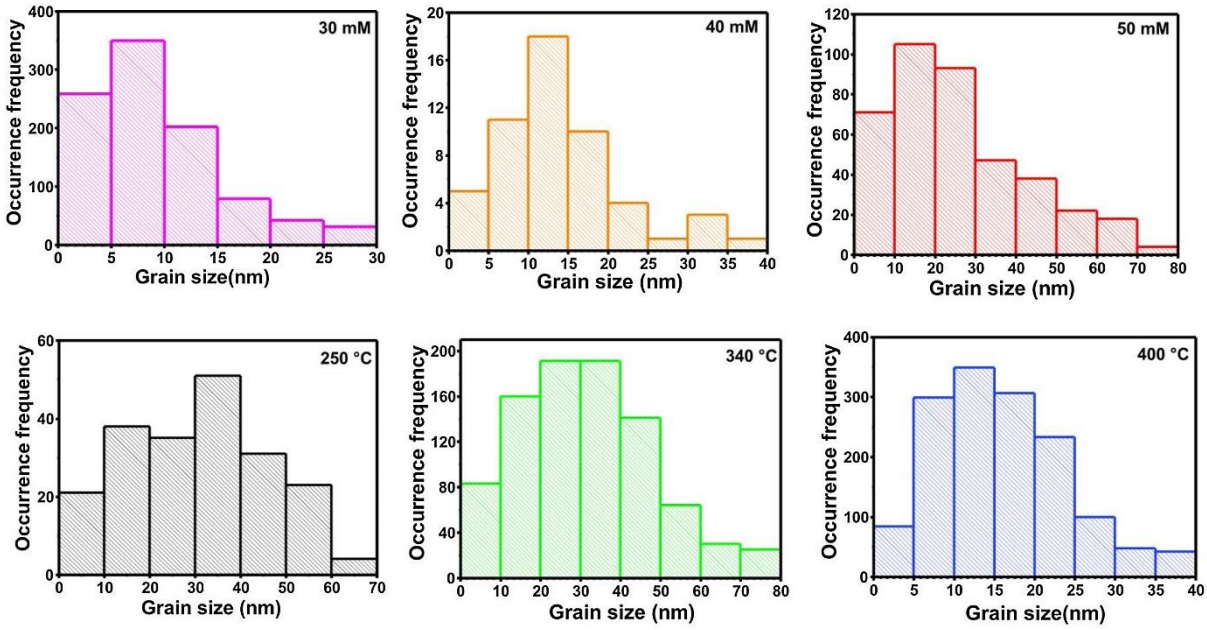


**Fig. 5.** Occurrence frequency of hematite NPs prepared at different deposition temperature and molar concentrations.

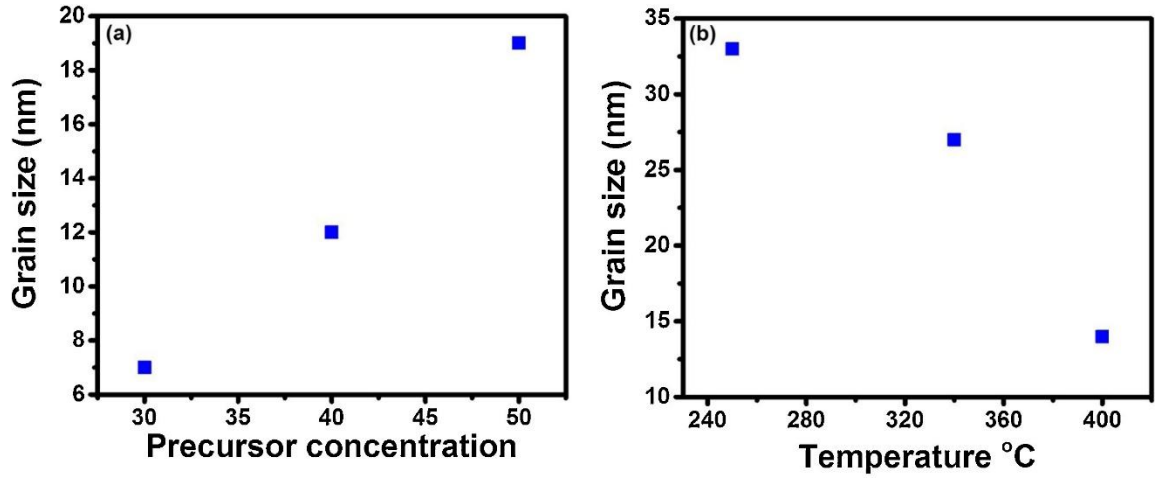


**Fig. 6.** Variation of grain size with, (a) precursor concentration and, (b) deposition temperature.

### 3.3. Optical properties

The absorbance of hematite thin films synthesized at different precursor concentrations and temperatures was measured using UV–vis spectroscopy. Hematite films were observed to absorb in the visible region with an absorption edge that ranged from 590 to 650 nm as shown in Fig. 7a and b. There was a red-shift in the absorption onset as the precursor concentrations increased from 30 to 50 mM and a blue shift in 40 mM film. On the other hand, a blue-shift of absorbance was observed as the deposition temperature was increased (Fig. 7b). This was due to an increase in grain sizes with precursor concentration and a decrease in grain size

with temperature. The decrease in grain sizes could have further led to a decrease in the film thickness. The optical band gap ($E_g$) was estimated using Tauc's equation as shown in Fig. 7c.

$$(\alpha h\nu)^n = A(h\nu - \mathrm{Eg}), \quad (5)$$

where $\alpha$ is the absorption coefficient, $A$ is a constant, $h\nu$ is the photon energy and $n$ the constant depending on the nature of transition [49]. From estimation, there was a decrease in the bandgap from 2.10 to 1.99 eV as the molar concentrations increased from 30 to 50 mM respectively. This could be due to an increase in grain sizes as the concentration was increased at a constant deposition temperature of 280 °C. However, the bandgap was observed to increase from 1.92 to 2.09 eV as the deposition temperature varies from 250 to 400 °C. This was a result of small grain size obtained at higher temperatures, leading to quantum confinement effect [50]. The decrease in bandgap with temperature could also be attributed to an increase in inter-atomic spacing which lowers the electron potential, enhancing phonon-electron interaction at higher temperatures [51]. Similar studies have been reported by Lassoued et al. using chemical precipitation method, with the variation of precursor concentration [52].

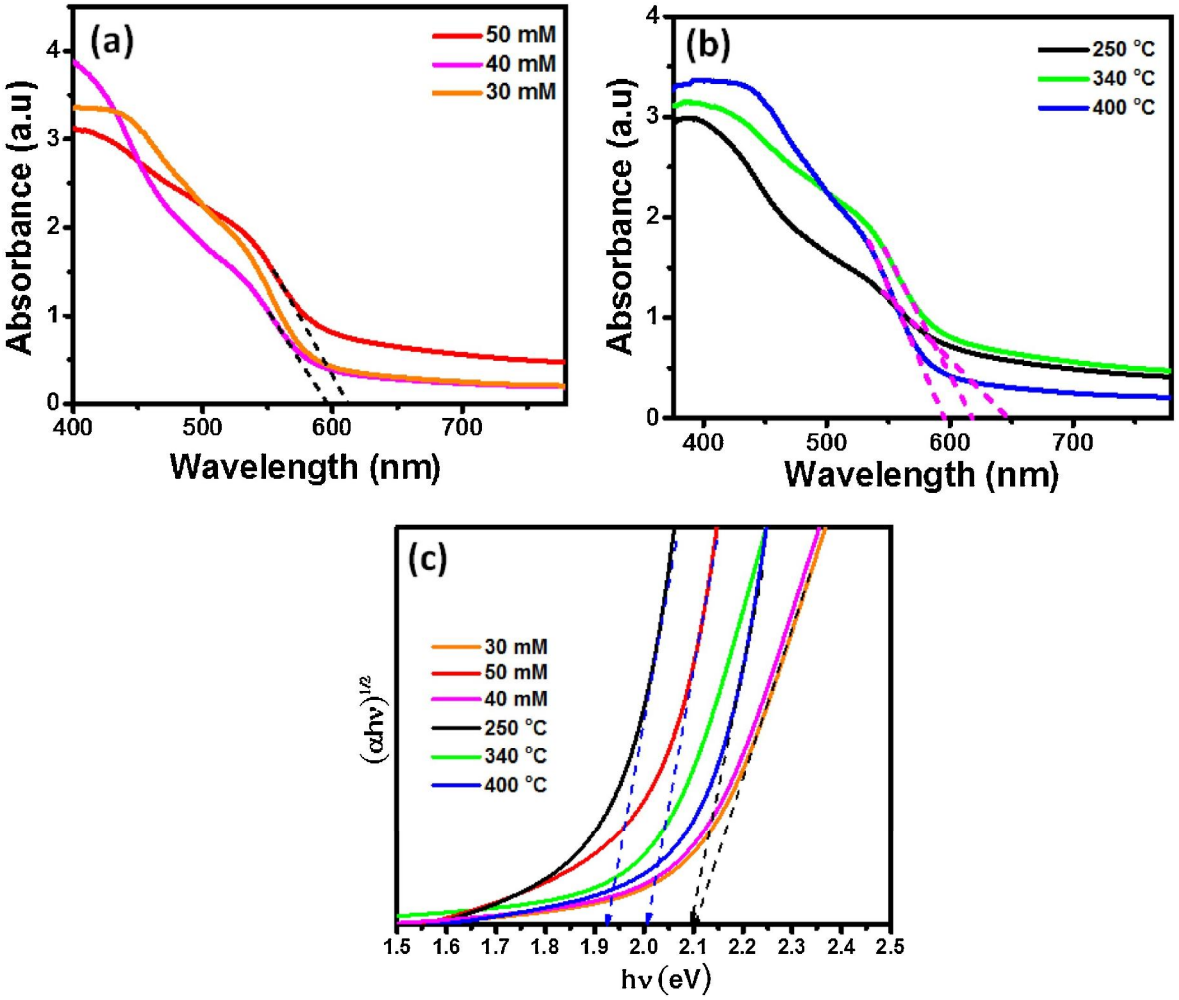


**Fig. 7.** Absorption edge of hematite thin films deposited at different (a) precursor concentrations, (b) deposition temperatures, (c) corresponding energy bandgaps of hematite thin films synthesized by spray pyrolysis.

### 3.4. Photocurrent measurements

The current–voltage curves for samples prepared at different precursor concentrations and temperatures were measured using 1 sun irradiation (Fig. 8) in a potentiostat setup (VersaSTAT 3F) explained in Section 3. The 50 mM precursor concentration samples reported the highest photocurrent density of 89 μA $cm^{-2}$ at 1.23 V *vs*. RHE (the water splitting potential). The current density was observed to decrease to 53 and 17 $\mu$A $cm^{-2}$ for 40 and 30 mM precursor concentration respectively. Additionally, for samples prepared at different temperatures, 400 °C recorded highest photocurrent density of 1.52 $\mu$A $cm^{-2}$ while 340 and 250 °C had low photocurrent densities of 1.03 and 0.78 $\mu$A $cm^{-2}$, respectively. The obtained current densities were however quite low as compared to the ones for different precursor concentrations. This could be due to smaller grain sizes, discussed in Section 3.2, which has an ultimate effect on the surface area the minority charge carrier travels before the possible e–h recombination. It could also be a result of the increase in thickness at lower deposition temperatures hence limiting the charge transfer from the FTO substrate to the top layer of hematite. There was an increase in the current density as the potential (V) *vs*. RHE was increased, and was observed in all the samples. However, these current densities are quite low as opposed to what has been reported by Lassoued et al. [52]. This has been caused by the poor conductivity of hematite, which requires doping, further nanostructuring, and functionalization. The dark current on all the samples is highly negligible up to 1.61 $V_{RHE}$ for films prepared at different precursor concentrations and 1.52 $V_{RHE}$ for samples at different temperatures, where the oxygen evolution starts. The properties of the hematite NPs obtained are summarized in Table 1.

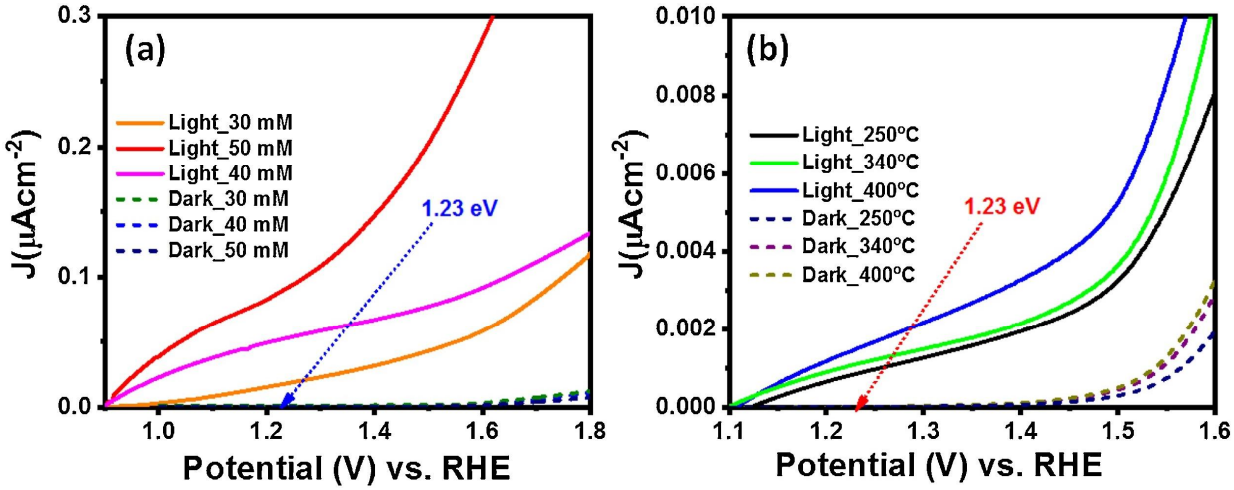


**Fig. 8.** Photocurrent density curves for hematite nanoparticles deposited at (a) different precursor concentration and, (b) deposition temperatures. 50 $mVs^{-1}$ scan rate and 1 M NaOH electrolyte were used.

**Table 1**. Summary of structural, optical and electrical properties of hematite thin films prepared by spray pyrolysis at different precursor concentrations and deposition temperatures.

| Sample | Average crystal size (nm) | Constant (a) (Å) | Lattice constant (b) (Å) | Bandgap (eV) | Current density $\mu$A cm$^{-2}$ |
|---|---|---|---|---|---|
| **30 mM** | 23.05 | 5.09 | 13.75 | 2.10 | 17 |
| **40 mM** | 27.63 | 5.03 | 13.75 | 2.06 | 53 |
| **50 mM** | 29.92 | 5.03 | 13.77 | 1.99 | 89 |
| **250°** | 38.11 | 5.01 | 13.69 | 1.92 | 1.52 |
| **340°** | 32.89 | 5.02 | 13.67 | 2.00 | 1.03 |
| **400°** | 23.97 | 5.01 | 13.68 | 2.09 | 0.78 |

### 3.5. Mott-Schottky analysis

A Mott-Schottky analysis was carried out in the dark with a frequency of 10,000 Hz based on Eq. (6).

$$\frac{1}{C^2} = \frac{2}{q\varepsilon\varepsilon_o N_D}(E - E_{\mathrm{FB}}) - \frac{\mathrm{kT}}{q}, \quad (6)$$

where $C$ is the space charge capacitance, $q$ is the electron charge, $\varepsilon$ is the dielectric constant of hematite which is 80, $\varepsilon_o$ dielectric permittivity of vacuum, $N_D$ is the carrier density, $E$ is the applied electrode potential, $E_{FB}$ is the flat band potential, $k$ is Boltzmann's constant and $T$ is the temperature. A linear graph is obtained from $C^{-2}$ *vs*. E which was used to estimate the flat band potential of the hematite nanostructures deposited at different temperatures and precursor concentrations. The flat band potential was then obtained from extrapolating the interception of the straight line with the *X*-axis (applied potential) from the slope. The donor density on the other hand was obtained from the slope of the graph.

Positive values for the Mott-Schottky analysis were obtained in all samples, an indication that electrons were the majority carriers hence n-type semiconductor. A lowest $E_{FB}$ of 0.023 V was obtained for the sample prepared at 250 °C. $E_{FB}$ which was in the range of 0.023 and 0.193 V was obtained for all the samples, with the 400 °C recording the highest. The donor density for all the samples was $10^{18}$ cm$^{-3}$. However, there was a slight increase in the $N_D$ for samples deposited at 50 mM and 400 °C that had $3.98 \times 10^{18}$ and $4.34 \times 10^{18}$ cm$^{-3}$ respectively, similar to what has been reported by Lopes et al., [53]. This increase in $N_D$ can be attributed to the change in thickness. Samples prepared at 400 °C could be thinner as compared to the other samples. This is due to deposition of the precursor in vapor form. Hematite generally suffers poor conductivity and hence the charge transfer is limited with the thicker samples. This also further explains the low PEC performance for these samples as shown in Fig. 9. Aiwu et al., has reported similar results on the effect of thickness of the films prepared by hydrothermal synthesis for solar water splitting [54]. The donor density and flat band potential obtained are summarized in Table 2.

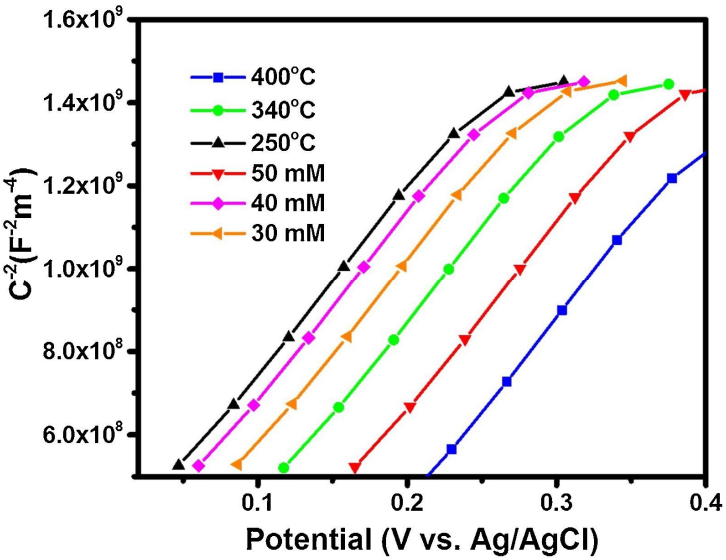


**Fig. 9.** Mott-Schottky plots of hematite nanoparticles deposited at different precursor concentration and deposition temperatures.

Table 2. Donor density and flat band potential of hematite NPs synthesized by spray pyrolysis.

| **Sample** | **Donor density ($\times 10^{18}$ cm$^{-3}$)** | **Flat band potential (V)** |
|---|---|---|
| **30 mM** | 2.09 | 0.084 |
| **40 mM** | 2.27 | 0.058 |
| **50 mM** | 3.98 | 0.162 |
| **250 °C** | 1.95 | 0.045 |
| **340 °C** | 3.77 | 0.116 |
| **400 °C** | 4.34 | 0.213 |

## 4. Conclusions

Chemical spray pyrolysis was successfully used to synthesize hematite NPs at different precursor concentrations (30, 40, and 50 mM) and deposition temperatures of 250, 340, and 400 °C. XRD studies revealed hematite phases with the diffraction peaks aligned in the respective $2\theta$ angles. The (104) and (110) indexed at 33.3° and 35.5° respectively, associated with the rhombohedral corundum structure of hematite, were dominant peaks in all the samples. From the study, the crystallinity improved with an increase in deposition temperatures and precursor concentrations. The grain sizes obtained from FESEM ranged from 7 to 19 nm, and 33 to 14 nm for different precursor concentrations and deposition temperatures, respectively. Grain sizes increased with an increase in molarity and decreased with an increase in temperature. The films were absorbing in the visible region. Bandgaps of 2.09, 2.06, and 1.99 eV were obtained for samples prepared at 30, 40, and 50 mM precursor concentrations, respectively while for different temperature films, 1.92, 2.00, and 2.09 eV for 250, 340, and 400 °C, respectively were achieved. However, the variation of precursor concentrations and deposition temperatures did not have much effect on the optical properties since the obtained $E_g$ were in the range of 1.90 and 2.20 eV, the standard bandgap for hematite. Photocurrent densities of 89, 53, 17 μA/cm$^2$ were obtained for 50, 40, and 30 mM respectively while for samples prepared at temperatures of 400, 340, and 250 °C recorded

photocurrent densities of 1.52, 1.02, and 0.78 μA/cm$^2$, respectively. The films prepared at 50 mM precursor concentration and 400 °C produced the maximum photocurrent densities. All the samples had a donor density of $10^{18}$ cm$^{-3}$ with a positive flat band potential that ranged from 0.045 and 0.213 V. The improvement in the PEC performance from these results is largely due to the cathodic shift of the flat band potential, that further improved the surface charge transport properties. The results provide a new understanding of the effect of precursor concentrations and deposition temperatures on the photocatalytic activity of hematite photoanodes prepared by spray pyrolysis. Future work will investigate the effect of the deposition height, spray pressure, and nozzle diameter variation during spray pyrolysis of hematite thin films on the photocatalytic applications.

## Data availability statement

The raw/processed data required to reproduce these findings cannot be shared at this time due to legal or ethical reasons, and also forms part of an ongoing study.

## Declaration of Competing Interest

The authors report no declarations of interest.

## Acknowledgment

The authors wish to thank the Department of Physics, University of Pretoria for support, the African Laser Center (ALC, J.S.N.), the National Research Foundation (NRF) grant No.N0115/115463 (SARChI, M.D.), and grant No. N00500/112085(T.P.J.K.) for financial support.

## References

[1] P.-Q. Wang, Y. Bai, P.-Y. Luo, J.-Y. Liu, Catal. Commun. 38 (2013) 82–85.

[2] S. Saritaş, E. Turgut, M. Kundakci, B. Gürbulak, M. Yildirim, Int. J. Sens. Netw. Data Commun. 6 (2017) 2.

[3] M. Hosenuzzaman, N. Rahim, J. Selvaraj, M. Hasanuzzaman, A.A. Malek, A. Nahar, Renew. Sustain. Energy Rev. 41 (2015) 284–297.

[4] B. Iandolo, B. Wickman, I. Zorić, A. Hellman, J. Mater. Chem. A 3 (2015) 16896–16912.

[5] T.J. Jacobsson, V. Fjällström, M. Edoff, T. Edvinsson, Energy Environ. Sci. 7 (2014) 2056–2070.

[6] D.A. Wheeler, G. Wang, Y. Ling, Y. Li, J.Z. Zhang, Energy Environ. Sci. 5 (2012) 6682–6702.

[7] S. Hu, C. Xiang, S. Haussener, A.D. Berger, N.S. Lewis, Energy Environ. Sci. 6 (2013) 2984–2993.

[8] A. Fujishima, K. Honda, Nature 238 (1972) 37. [9] S. Reda, M. Khairy, M. Mousa, Arab. J. Chem. 13 (2020) 86–95. [10] P. Subramanyam, B. Meena, G.N. Sinha, M. Deepa, C. Subrahmanyam, Int. J. Hydrogen Energy 45 (2020) 7706–7715.

[11] T. Soltani, A. Tayyebi, B.-K. Lee, Catal. Today 340 (2020) 188–196.

[12] D. Chen, Z. Liu, Z. Guo, W. Yan, M. Ruan, Chem. Eng. J. 381 (2020) 122655.

[13] J.F. de Brito, F. Tavella, C. Genovese, C. Ampelli, M.V.B. Zanoni, G. Centi, S. Perathoner, Appl. Catal. B: Environ. 224 (2018) 136–145.

[14] B.-S. Wang, R.-Y. Li, Z.-Y. Zhang, X.-L. Wu, G.-A. Cheng, R.-T. Zheng, et al., Catal. Today 321 (2019) 100–106.

[15] A.S. Reddy, J. Kim, Appl. Surf. Sci. 513 (2020) 145836.

[16] G. Li, W. Zhang, J. Hou, T. Li, P. Li, Y. Wang, G. Liu, K. Wang, Mater. Today Commun. 23 (2020) 100933.

[17] S. Mishra, P.K. Maurya, A.K. Mishra, Mater. Today Commun. (2020) 101270.

[18] C. Li, Z. Luo, T. Wang, J. Gong, Adv. Mater. 30 (2018) 1707502.

[19] F. Le Formal, N. Tetreault, M. Cornuz, T. Moehl, M. Grätzel, K. Sivula, Chem. Sci. 2 (2011) 737–743.

[20] A.G. Tamirat, W.-N. Su, A.A. Dubale, C.-J. Pan, H.-M. Chen, D.W. Ayele, J.-F. Lee, B.-J. Hwang, J. Power Sources 287 (2015) 119–128.

[21] T. Mari no-Otero, M. Oliver-Tolentino, M.A. Aguilar-Frutis, G. Contreras-Martínez, E. Pérez-Cappe, E. Reguera, Int. J. Hydrogen Energy 40 (2015) 5831–5836.

[22] K.L. Hardee, A.J. Bard, J. Electrochem. Soc. 124 (1977) 215–224.

[23] S. Kment, F. Riboni, S. Pausova, L. Wang, L. Wang, H. Han, Z. Hubicka, J. Krysa, P. Schmuki, R. Zboril, Chem. Soc. Rev. 46 (2017) 3716–3769.

[24] L.M. Peter, K.U. Wijayantha, A.A. Tahir, Faraday Discuss. 155 (2012) 309–322.

[25] B. Eftekharinia, A. Moshaii, A. Dabirian, N.S. Vayghan, J. Mater. Chem. A 5 (2017) 3412–3424.

[26] D.K. Bora, A. Braun, E.C. Constable, Energy Environ. Sci. 6 (2013) 407–425.

[27] A.G. Tamirat, J. Rick, A.A. Dubale, W.-N. Su, B.-J. Hwang, Nanoscale Horiz. 1 (2016) 243–267.

[28] F. Urbain, P. Tang, V. Smirnov, K. Welter, T. Andreu, F. Finger, J. Arbiol, J.R. Morante, ChemSusChem 12 (2019) 1428–1436.

[29] C. Feng, S. Fu, W. Wang, Y. Zhang, Y. Bi, Appl. Catal. B: Environ. 257 (2019) 117900.

[30] S. Gahlawat, J. Singh, A.K. Yadav, P.P. Ingole, Phys. Chem. Chem. Phys. 21 (2019) 20463–20477.

[31] C.-Y. Chiang, J. Epstein, A. Brown, J.N. Munday, J.N. Culver, S. Ehrman, Nano Lett. 12 (2012) 6005–6011.

[32] F.L. Souza, K.P. Lopes, E. Longo, E.R. Leite, Phys. Chem. Chem. Phys. 11 (2009) 1215–1219.

[33] D.K. Bora, A. Braun, S. Erat, A.K. Ariffin, R. Löhnert, K. Sivula, J. Töpfer, M. Grätzel, R. Manzke, T. Graule, et al., J. Phys. Chem. C 115 (2011) 5619–5625.

[34] D.N. Muche, T.M. dos Santos, G.P. Leite, M.A. Melo Jr., R.V. Gonçalves, F.L. Souza, Mater. Lett. 254 (2019) 218–221.

[35] H. Bemana, S. Rashid-Nadimi, Surf. Interfaces 14 (2019) 184–191.

[36] M. Allieta, M. Marelli, F. Malara, C.L. Bianchi, S. Santangelo, C. Triolo, S. Patane, A.M. Ferretti, Š. Kment, A. Ponti, et al., Catal. Today 328 (2019) 43–49.

[37] R. Kant, S. Pathak, V. Dutta, Sol. Energy Mater. Sol. Cells 178 (2018) 38–45.

[38] S. Shinde, R. Bansode, C. Bhosale, K. Rajpure, J. Semicond. 32 (2011) 013001.

[39] N. Lehraki, M. Aida, S. Abed, N. Attaf, A. Attaf, M. Poulain, Curr. Appl. Phys. 12 (2012) 1283–1287.

[40] J.S. Nyarige, T.P. Krüger, M. Diale, Phys. B: Condens. Matter 581 (2019) 411924. [41] J.S. Nyarige, T.P. Krüger, M. Diale, Surf. Interfaces 18 (2020) 100394.

[42] E.S. Cho, M.J. Kang, Y.S. Kang, Phys. Chem. Chem. Phys. 17 (2015) 16145–16150.

[43] J. Hua, J. Gengsheng, Mater. Lett. 63 (2009) 2725–2727.

[44] M. Hakimi, M. Alikhani, J. Inorg. Organomet. Polym. Mater. 30 (2020) 504–512.

[45] J. Hargreaves, Catalysis, Struct. React. 2 (2016) 33–37.

[46] Y. Meftah, D. Bekker, B. Benhaoua, A. Rahal, A. Benhaoua, A. Hamzaoui, Digest J. Nanomater. Biostruct. 13 (2018) 465–474.

[47] M. Sharma, S. Murugavel, D.K. Shukla, F.M. De Groot, J. Phys. Chem. C 122 (2018) 9292–9301.

[48] D.E. Fouad, C. Zhang, H. El-Didamony, L. Yingnan, T.D. Mekuria, A.H. Shah, Results Phys. 12 (2019) 1253–1261.

[49] J. Gao, Q. Zhao, Y. Sun, G. Li, J. Zhang, D. Yu, Nanoscale Res. Lett. 6 (2011) 1–6.

[50] C. Garoufalis, P. Poulopoulos, N. Bouropoulos, A. Barnasas, S. Baskoutas, Phys. E: Low-dimens. Syst. Nanostruct. 89 (2017) 67–71.

[51] P.K. Sarswat, M.L. Free, Phys. Status Solidi (A) 208 (2011) 2861–2864.

[52] A. Lassoued, B. Dkhil, A. Gadri, S. Ammar, Results Phys. 7 (2017) 3007–3015.

[53] T. Lopes, L. Andrade, F. Le Formal, M. Gratzel, K. Sivula, A. Mendes, Phys. Chem. Chem. Phys. 16 (2014) 16515–16523.

[54] A. Pu, J. Deng, Y. Hao, X. Sun, J. Zhong, Appl. Surf. Sci. 320 (2014) 213–217.